Title

Analysis of Molecular Concentration and Brightness from Fluorescence Fluctuation Data with an Electron Multiplied CCD Camera

Journal

Biophysical Journal, 95(11)

ISSN

0006-3495

Authors

Unruh, Jay R
Gratton, Enrico

Publication Date

2008-12-01

DOI

10.1529/biophysj.108.130310

Analysis of Molecular Concentration and Brightness from Fluorescence Fluctuation Data with an Electron Multiplied CCD Camera

Jay R. Unruh and Enrico Gratton
Laboratory for Fluorescence Dynamics, Department of Biomedical Engineering, University of California, Irvine, California

ABSTRACT We demonstrate the calculation of particle brightness and concentration from fluorescence-fluctuation photon-counting statistics using an electron-multiplied charge-coupled device (EMCCD) camera. This technique provides a concentration-independent measure of particle brightness in dynamic systems. The high sensitivity and highly parallel detection of EMCCD cameras allow for imaging of dynamic particle brightness, providing the capability to follow aggregation reactions in real time. A critical factor of the EMCCD camera is the presence of nonlinearity at high intensities. These nonlinearities arise due to limited capacity of the CCD well and to the analog-to-digital converter maximum range. However, we show that the specific camera we used (with a 16-bit analog-to-digital converter) has sufficient dynamic range for most microscopy applications. In addition, we explore the importance of camera timing behavior as it is affected by the vertical frame transfer speed of the camera. Although the camera has microsecond exposure time for illumination of a few pixels, the exposure time increased to milliseconds for full-field illumination. Finally, we demonstrate the ability of the technique to follow concentration changes and measure single-molecule brightness in real time in living cells.

INTRODUCTION

In the past 10 years, there has been a virtual explosion in the number of fluorescence fluctuation techniques available to researchers for analysis of particle brightness, concentration, and diffusion coefficient in complex samples. Perhaps the greatest benefit of these techniques lies in their capability to observe molecular interactions in living cells. It is important to note that fluctuation techniques are uniquely sensitive to weak homointeractions that play an important role in rapid signaling events. Förster resonance energy transfer (FRET) measurements make it possible to look at heterogeneous interactions, but require the successful incorporation of multiple fluorophores into a living sample. In addition, there is no guarantee that FRET will occur between two interacting species due to the large size of biological chromophores. Also, FRET has limited or no sensitivity to distinguish between aggregates with more than two partners. The need for techniques to study molecular interactions directly inside living cells has been highlighted recently by advances in systems biology and modeling. These techniques rely on characterization of biological binding partners for the development of network models for cellular function.

In the early 1990s, Qian and Elson developed a particular version of fluorescence fluctuation spectroscopy, moment analysis, that used the statistics of fluorescence fluctuations to determine particle concentration and brightness while omitting the time dependence of the signals (1). That study calculated the contribution to the first three moments from Poisson shot noise to correct for these fluctuations in the analysis. In 1999, Chen et al. developed the photon-counting histogram analysis (PCH), and Kask et al. developed the fluorescence intensity distribution analysis, which accounted for shot noise through fitting of the data (2). In 2004, Joachim Mueller developed an equivalent method, termed fluorescence cumulant analysis, which is a general extension of moment analysis into higher-order moments with error analysis (3). This allows for the rapid calculation of molecular concentration and brightness without the complicated computation involved in other approaches. Recently, our group applied moment analysis with correction for shot noise in each pixel of a photon-counting confocal image, allowing for the mapping of particle aggregation in a spatial manner. This technique, termed ''N and B analysis'' has proven to be an invaluable tool for mapping out the cellular location of signaling processes (4). More recently, this technique was extended for use with analog detectors, which dominate the confocal microscopy field (5).

This work intends to explore the use of the N and B analysis technique with an important subset of analog detection systems—the electron-multiplied charge-coupled device (EMCCD) camera. These devices have proven themselves for use in ultralow-light imaging conditions, becoming the standard for single-molecule imaging of surface-bound proteins or surface reactions via the total internal reflection fluorescence (TIRF) imaging modality. In addition, the parallel character of detection with these systems allows for the most rapid large-scale imaging of any technique and also forms the basis for rapid confocal techniques like spinning-disk microscopy.

These cameras have been successfully employed under several circumstances for fluorescence correlation spectroscopy in both the spatial correlation modality (6) and the

Submitted February 29, 2008, and accepted for publication August 13, 2008.

Address reprint requests to Enrico Gratton, University of California, Irvine, Biomedical Engineering, Irvine, CA 92697. Tel.: 949-824-2674; E-mail: egratton22@yahoo.com.

Editor: Taekjip Ha.

0006-3495/08/12/5385/14 $2.00

doi: 10.1529/biophysj.108.130310

temporal correlation modality (7–10). In the spatial correlation modality, the spatial average of the molecular brightness is measured over a minimum of several point-spread functions. This limits the spatial resolution of brightness measurements, but also enhances the signal/noise ratio of such a measurement. In the temporal correlation modality, the spatial extent of the acquired correlation stack is limited by the readout speed of the camera. For example, the 512 × 512 chip cameras have a maximum full-frame rate of 30 fps, corresponding to a time resolution of 33 ms, but with a much smaller region of interest, this time resolution can be increased to a few milliseconds. One study employed the ultrafast 128-pixel camera for these measurements (7). Other studies have limited themselves to slower-moving objects or small regions of interest. It is also important to note that temporal correlation analysis with these systems requires a significant investment in signal/noise due to the nonlinear least-squares fitting requirements of correlation analysis.

This work seeks to overcome these challenges with a ''fit-free'' moment analysis approach to the determination of molecular brightness and concentration at each pixel in an image with minimal required signal/noise. This approach is limited not by the frame rate of the camera but by its exposure resolution, thereby maximizing the analysis size for such measurement. In addition, we demonstrate that by changing the exposure time of the camera it is possible to capture the time dependence of molecular fluctuations using techniques described previously.

Despite their advantages, EMCCD detectors present some unique challenges. The presence of charge-well saturation and leakage gives rise to unique statistics that must be understood to accurately calculate the particle concentration and brightness. In addition, the exposure timing of these cameras is complex and strongly influenced by the frame transfer characteristics of the camera. We show that the judicious choice of acquisition parameters results in measurements that have high dynamic range and time resolution, maximizing the capabilities of the camera system. Finally, we demonstrate the ability to resolve the relative concentration and brightness of single enhanced green fluorescent protein (EGFP) molecules in living cells within a few seconds, allowing for real-time observation of brightness and concentration dynamics.

THEORY

Following Qian and Elson, our previous work defined N and B as follows (4):

$$N = \frac{(\langle I\rangle - \mathit{offset})^2}{\sigma^2 - \sigma_0^2},\ B = \frac{\sigma^2 - \sigma_0^2}{\langle I\rangle - \mathit{offset}}. \tag{1}$$

Here, *offset* is the intensity offset of the detection electronics and σ_0^2 is the readout noise variance of the detection electronics. The above equations are based purely on signal fluctuations in a given pixel. Therefore, shot noise is not separated from particle number fluctuation, and these expressions do not give the true molecular number (denoted n) and brightness (denoted ε). In the appendix, we show that the variance and average intensity for an analog detector are given as follows in terms of molecular brightness and number of molecules:

$$\sigma^2 - \sigma_0^2 = SG\varepsilon n + G^2\gamma\varepsilon^2 n \tag{2}$$

$$\langle I\rangle - \mathit{offset} = G\varepsilon n, \tag{3}$$

where G is the analog gain in digital levels (DL)/photon, S is the slope of the intensity versus variance plot for a constant intensity at the analog detector, γ is a factor relating to the shape of the pixel detection volume. Using these expressions, it is straightforward to calculate B in terms of ε:

$$\frac{B}{S} = \frac{G}{S}\gamma\varepsilon + 1. \tag{4}$$

Therefore, the quantity B/S is linearly dependent on ε. Experimentally, ε is a complex function of laser intensity and the detection efficiency of the system. Therefore, it is only important that we determine the relative value of ε for a specific detection modality. We can calibrate this value using a particle with known brightness. This allows us to simplify Eq. 4 to

$$B/S = \varepsilon' + 1, \tag{5}$$

where ε' is proportional to ε. The solution for n is more complex, but as with ε we are generally only interested in the relative value of n, not its absolute value. One can then show that: $n'\varepsilon' = (\langle I\rangle - \mathit{offset})/S$. Note that $n' = n/\gamma$, which is the reciprocal of the $G(0)$ term from fluorescence correlation spectroscopy (FCS) analysis.

As was mentioned above, only the relative brightness will be considered in this work. Nevertheless, for completeness, we will attempt to approximate the γ factor according to the definition given by Müller (3). For diffusion in three dimensions in and out of a TIRF field, the point-spread function has been described as an exponential in z and a Gaussian in x and y. For this point-spread function, the γ factor is 0.25. It is important to note that this is only an approximation. Several studies have suggested that the TIRF point-spread function is better approximated by a multiexponential function in z. In this case, the γ factor is weakly dependent on the shape of the point-spread function, but similar to what is seen for a single-exponential point-spread function; therefore, we will retain 0.25 as an estimate only for rough calculations. For TIRF or brightfield studies on a membrane, it is often assumed that the membrane thickness is significantly less than the axial dimension of the point-spread function. This would produce a 2D Gaussian point-spread function with a γ factor of 0.5. This approximation is only as good as the approximation of a thin membrane. If undulations in the membrane are larger than the z-dimension of the point-spread function, this will be an overestimate. It should therefore only be used for rough calculations, as with the TIRF approximation.

It is important to note the specific contribution of background to this signal. Background here is defined as constant (relative to the timescale of the fluctuations) signal containing

only shot noise. This contribution must be estimated a priori from a control experiment. The variance of the background component can be shown to be $S\langle I\rangle$. Since variance is additive, this can be simply subtracted from the overall variance. The same can be done for the average intensity. It is easy to show that the presence of background will reduce the apparent brightness and increase the apparent number of molecules. When large immobile aggregates are present in an image, they will generally appear much brighter than small fluctuating molecules or even small aggregates. Using our expression for brightness, these regions of the image will show up as high intensity with zero brightness. This can be used as a measure of mobility (4).

Given these developments, we now have a straightforward recipe for performing number and brightness analyses. The offset and σ_0^2 parameters can be determined from a dark image or a region of the acquired image without mobile particles. The S parameter is determined from a plot of variance versus intensity for a constant source of light. It is tempting to calculate ε' and n' for every pixel in an image. Nevertheless, for most single molecules, ε' lies quite close to zero. Therefore, the statistical error of the measurement, especially for a very few frames, will lead to infinite or negative values of n'. A 2D histogram of B/S vs. $(\langle I\rangle - \mathit{offset})/S$ represents a plot of ε' vs. $\varepsilon' n'$. This plot contains all of the information necessary to characterize the system in question without the physically unreasonable values of n'.

Although the analog solution for number and brightness is quite simple, it would be ideal to eliminate shot noise from the analysis. If, for example, two simultaneous measurements can be done on the same sample, their shot noise and readout noise will be uncorrelated. As a result, only the molecular fluctuations will be correlated and the covariance is representative only of the particle number fluctuations. This can be accomplished trivially with a 50% beam splitter, as is often done to eliminate afterpulsing from fast autocorrelation analyses. Nevertheless, this uses up valuable camera pixels and reduces the signal intensity by half.

For fast cameras, it is possible to sample faster than the diffusion time of the molecule of interest. In this case, there is a temporal redundancy present in that the molecule does not move significantly between subsequent frames. Since the read noise and shot noise are not correlated in time, the covariance of subsequent frames in time is given by the second term in Eq. 2, and B is given by

$$B = G\gamma\varepsilon = \varepsilon'. \tag{6}$$

Thus, B is directly proportional to ε for this analysis. Similarly, $n'\varepsilon' = \langle I\rangle - \mathit{offset}$, where $n' = n/\gamma$. Therefore, this analysis is independent of S, and B is in units of the gain of the system, greatly simplifying the analysis. This is similar to calculating the extrapolated $G(0)$ point of the FCS autocorrelation function and therefore will be referred to as $G1$ analysis. Of course, this is only true in the limit of fast sampling relative to the diffusion time.

In the same way, one could use the spatial redundancy of the system, assuming that shot noise and read noise are not correlated in neighboring pixels. Given a great enough degree of spatial oversampling, each particle will be visible in several pixels simultaneously. Here, one must be quite careful that this analysis is done in the orthogonal direction to the readout coordinate of the camera. This is because the analog system will inevitably have some damping time constant that correlates slightly from pixel to pixel in the horizontal direction during the readout process. This can easily be identified by calculating the spatial correlation of the dark noise of the camera. The mathematical analysis is identical to the case of temporal oversampling, except that it is the covariance of neighboring pixels that is calculated rather than the covariance of subsequent time points. This is identical to the calculation of the first point of the spatial autocorrelation function in the y dimension and therefore will be referred to as $G1y$ analysis throughout this article. Both of these analysis methods sacrifice signal/noise in exchange for simplicity. In the case of temporal oversampling, the effect is to reduce the number of photons collected per analysis frame by a factor of 2, thus reducing the signal/noise by a factor of 1.4. In the case of spatial oversampling, the penalty is instead a factor of 4, since spatial oversampling affects both the x and y dimensions. Here, the signal/noise is penalized by a factor of 2. High amounts of spatial oversampling are commonly used to identify single molecules via image correlation analysis (11), so it is not likely that this will be a significant limitation.

Wu and Mueller have described the exposure time dependence of the molecular brightness as it applies to fluorescence cumulant analysis (12). The following equation relates the brightness to a binning function, $B_2(T_r)$:

$$\frac{\varepsilon(T)}{T} \propto \frac{B_2(T_r)}{T^2}, \tag{7}$$

where T is the exposure time and $T_r = T/\tau_D$ is the exposure time in units of the radial diffusion time ($\tau_D = \omega_0^2/4D$). The binning function is given as follows (12):

$$B_2(T_r) = 2\int_0^{T_r} G(\tau_r)(T_r - \tau_r)d\tau_r, \tag{8}$$

where $G(\tau_r)$ is the normalized autocorrelation function in units of the diffusion time ($\tau_r = \tau/\tau_D$). We have chosen to plot the ratio of brightness to exposure time because this function closely resembles the autocorrelation function. At short exposure times relative to the diffusion time, the function approaches a constant, and at long exposure times, this function approaches zero. For one-photon confocal detection, the point-spread function is approximated by the 3D Gaussian function and the autocorrelation function has its familiar form:

$$G(\tau_r)_{3DG} = \frac{1}{(1+\tau_r)\sqrt{1+r^2\tau_r}}, \tag{9}$$

where r is the ratio between the radial and axial dimensions of the focal volume. This gives rise to the binning function

$$B_2(T_r)_{3DG} = \frac{4(1-y)}{1-a} + \frac{2(1+T_r)}{\sqrt{a}} \ln\left[\frac{(y-\sqrt{a})(1+\sqrt{a})}{(y+\sqrt{a})(1-\sqrt{a})}\right], \tag{10}$$

where we have introduced $y = \sqrt{1+r^2T_r}$ and $a = 1-r^2$ for brevity. For TIRF illumination, we can approximate the point-spread function by a Gaussian in the radial direction and an exponential with average height, d, in the axial direction. Hassler et al. (13) showed that the autocorrelation is then given by

$$G(\tau_r)_{TIRF} = \frac{(1-\tau_r/2)\exp(\tau_r/4)\mathrm{erfc}(\sqrt{\tau_r/4}) + \sqrt{\tau_r/\pi}}{1+\tau_r/r^2}. \tag{11}$$

Here, τ_r is defined relative to the axial diffusion time ($\tau_r = \tau/\tau_z$), where $\tau_z = d^2/4D$. As before, r is the ratio between radial and axial dimensions of the focal volume. There is no simple analytical solution for the binning function here, so it was calculated by numerical integration.

MATERIALS AND METHODS

Materials

Dioleoylphosphatidylcholine (DOPC) was obtained from Avanti Polar Lipids (Alabaster, AL). DiO-C16 and 110 nm fluospheres were obtained from Molecular Probes (Eugene, OR). FITC-dextran was obtained from Sigma (St. Louis, MO). Purified monomeric EGFP (14) was obtained from Michelle Digman (Department of Biomedical Engineering, University of California, Irvine, CA). Chinese hamster ovary (CHO) K1 cells were maintained in low-glucose D-MEM supplemented with penicillin/streptomycin and 10% fetal bovine serum (Invitrogen, Carlsbad, CA). The cells were transiently transfected with the growth-associated protein (GAP)-EGFP plasmid (obtained from Alan Horwitz, Department of Cell Biology, University of Virginia (15)) using Lipofectamine 2000 (Invitrogen) 24 h before imaging. Imaging was accomplished at 37°C with a Warner Instruments stage incubator (Warner Instruments, Hamden, CT).

Supported planar bilayer

Supported planar bilayers (SPBs) were generated according to the protocol of Burns and co-workers with minor modifications (16). Briefly, 1.25 mg of DOPC in chloroform was mixed with the appropriate amount of DiOC16, also in chloroform. The chloroform was evaporated under a stream of dry nitrogen. The sample was further dried for 1 h in a lyophilizer. After resuspension in 500 mL of buffer (100 mM NaCl and 40 mM sodium phosphate, pH 7.4) by vortexing, the sample was subjected to three freeze-thaw cycles. The sample was then extruded through two stacked 100-nm polycarbonate filters using the Avestin extruder. Vesicle size was confirmed by FCS of the labeled vesicles.

Glass coverslips (Corning, Corning, NY) were cleaned in a piranha solution created by mixing seven parts x-grade H_2SO_4 with 3 parts x-grade hydrogen peroxide. Coverslips were immersed in this solution for 1 h and rinsed copiously with ultrapure water. Before SPB deposition, coverslips were dried under a stream of nitrogen. Vesicles were pipetted onto the slide and then diluted 1:5 with imaging buffer (150 mM NaCl, 50 mM sodium phosphate, and 1.5 mM sodium azide, pH 7.4). After 15 min of incubation, the SPB was washed vigorously with imaging buffer.

Fluorescence microscopy

Images were acquired at the image plane of an Olympus IX81 (Olympus America, Center Valley, PA) microscope with a Cascade 512B EMCCD camera equipped with a Dual View image splitter (Photometrics (a division of Roper Scientific), Tucson, AZ). Electron multiplication was used at the maximum level for all experiments shown here. Confocal mode experiments were done with the laser collimated to overfill the back aperture of the objective to form a diffraction-limited spot within the sample. These experiments were done with a 60× 1.2 NA water objective (Olympus, Melville, NY) and the 488 line of an argon ion laser (Melles Griot (a division of CVI Laser), Carlsbad, CA) with a power at the sample of ~10 kW/cm^2. A single 16 × 16-μm pixel of the camera was used as a pinhole for the measurement. This corresponds to ~0.5 airy diameter units ($d_{airy} = 1.22\lambda M/NA$). Brightfield mode was accomplished by focusing a laser beam at the center of the back aperture of a 60× 1.45 NA oil objective (Olympus) with a 20-cm lens, so that a collimated beam was emitted from the front aperture of the objective. Here, the laser intensity at the image plane was ~50 W/cm^2. TIRF mode imaging was accomplished by translating the focused brightfield beam to the edge of the objective aperture.

Camera exposure calibration

Camera exposure time and frequency were measured using heterodyning with a 471-nm frequency-modulated diode laser from ISS (Champaign, IL) modulated with a pulse generator (PM5786B, Fluke, Everett, WA). The laser was collimated overfilling the back aperture of the objective so that a diffraction-limited spot was formed within the focal plane. A concentrated solution of fluorescein was used as a fluorescent reporter of the laser intensity. The laser pulse was set to 100 μs for all experiments. For each camera acquisition frequency, the laser frequency was set slightly lower so that the camera exposure behavior could be observed on the timescale of many acquisition frames.

Simulations

Simulations were calculated using a program written in-house. The program updates the positions of particles randomly distributed in two dimensions with a Gaussian random number generator with standard deviation $\sqrt{2DT}$, where T is the period of the simulation and D is the diffusion coefficient. For each frame, a Gaussian intensity distribution was superimposed on the position of each particle with amplitude corresponding to the average intensity/frame. A Poisson random number generator was then used to calculate the photon counts corresponding to each intensity. For analog simulations, a multiexponential random number was calculated for each photon in a pixel according to the desired single-photon response. These were then added together to get the analog distribution. Finally, a Gaussian random number and an offset were added to each pixel to simulate the analog offset and read noise.

Data analysis

Data analysis was performed as described in the Theory section, using either software written in-house or SimFCS (Laboratory for Fluorescence Dynamics, Irvine, CA). For all 2D histogram analyses, the average and variance images were smoothed before calculation of the 2D histogram. The smoothing was a 3 × 3-pixel spatial moving average, with the center pixel weighted twice as much as the surrounding pixels.

RESULTS

Simulations

Fig. 1 *A* shows simulations for 2D diffusion of a particle with a diffusion coefficient of 2 μm^2/s. There are ~1.6 particles

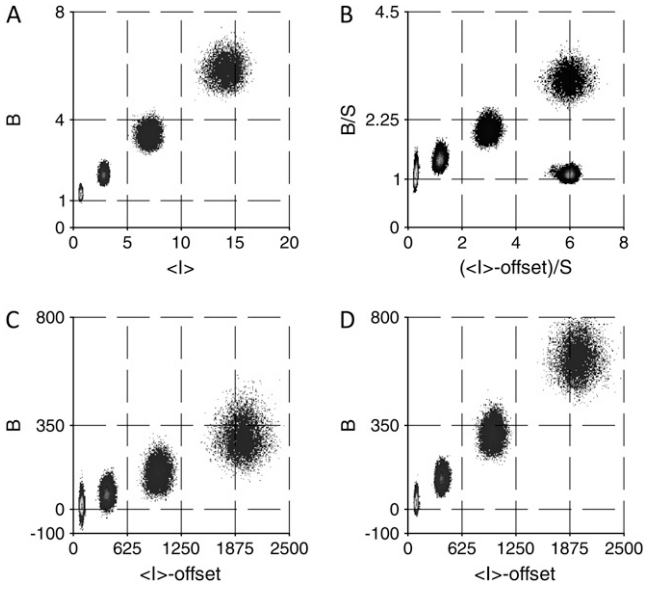

FIGURE 1 B/S versus $\langle I\rangle - offset/S$ plots for photon-counting simulations (*A*) and simulations with the same analog noise as the Cascade camera (*B–D*). (*C* and *D*) $G1$ and $G1y$ analyses, respectively, of the simulation. All simulations used 2D diffusion with 1250 molecules in a 3.5 × 3.5-μm box, except for the high-intensity, low-brightness point in *B*, which used 25,000 molecules in the same box size. The diffusion coefficient was 2 $\mu m^2/s$, with a frame rate of 200 frames/s. Each simulation was run for 100 frames with a frame resolution of 128 × 128 pixels. Brightness values were 0.5, 2, 5, and 10 cpfm.

per diffraction-limited area. Fig. 1 *B* shows this same plot for data with the same single-photon pulse height distribution as the Cascade 512B (see Appendix). Fig. 1 also shows the *B* versus $(\langle I\rangle - offset)/S$ plot for $G1$ and $G1y$ analyses of the analog simulated data. We also performed simulations at the lowest brightness point with no read noise and achieved essentially the same result (data not shown). Finally, we performed simulations with the lowest brightness and concentration increases to produce intensities equivalent to the brightest data point. Here, the error in the measured brightness has decreased dramatically and is approximately the same as for the photon-counting measurement. The error in the photon-counting measurement at the same brightness and concentration does not differ from the error at low concentration (data not shown).

Pixel uniformity

The ease of statistical calculations is strongly related to the uniformity among camera pixels. Since our calculations involve the relationship between detector variance and overall intensity, we tested the pixel uniformity by calculating the slope of this relationship for all pixels at intermediate intensity (1/10 of output range). Variances and intensities were calculated using an image stack size of 1024 frames. The microscope transmission lamp was used as a constant and uniform source of light. The contribution from long-term lamp-intensity fluctuations was assessed by subtracting a moving average with a period of three images (shot noise is instantaneous and therefore is not affected by the subtraction). The results were not changed significantly, indicating that lamp fluctuations do not contribute to the variance. The plot of the variance versus intensity slope at each pixel is shown in Fig. 2 *A*. The standard deviation among pixels is 7, with an average slope of 114.

The range of variance versus intensity slope values could be due to either a random distribution of static pixel characteristics, or to random error in measuring the slope. To test this, we split the image series in half and calculated the slope from each image set. Fig. 2 *B* shows the 2D scatter histogram of the slopes from the two experiments. The distribution is nicely round, indicating that the two experiments were independent of one another. The Pearson correlation coefficient is 0.006, reinforcing this conclusion. This indicates that the variation in slope from the pixels is not a result of static variation in pixel character but rather of random error in measuring the slope.

At high intensities (three-fourths of the output range) and low amplifier gain, significant saturation is observed from the system (see below). Therefore, it is of interest to characterize the uniformity in saturation intensity across pixels. The slope of intensity versus variance is also a good measure of this characteristic. As a result, we repeated the above experiments

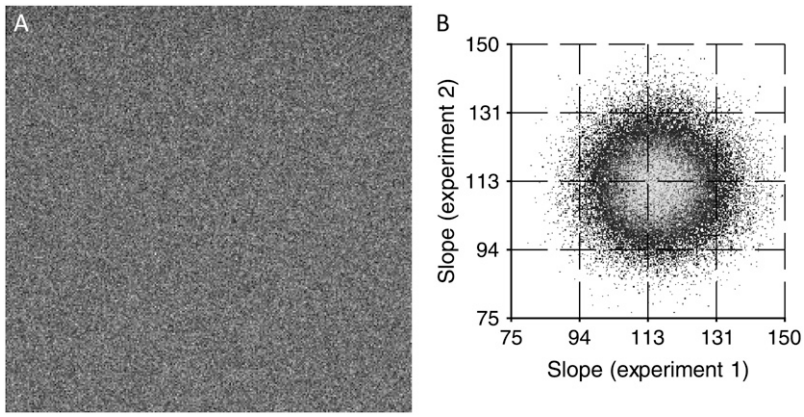

FIGURE 2 (*A*) Image of variance versus intensity slope for the Cascade camera. Image size is 68 μm. (*B*) Two-dimensional correlation scatter plot for two measurements of the variance versus intensity image.

at higher intensity. The resulting slope was −67, indicating that we have indeed reached saturation, with a standard deviation of 33. Again we performed correlation between two identical experiments. Here, the Pearson coefficient was 0.06, indicating that there is a small amount of correlation. Nevertheless, the 2D scatter histogram remains relatively round, indicating that the correlation is small (data not shown).

Detection linearity and saturation

As was mentioned before, the determination of particle number and brightness is dependent on the linearity between intensity and variance. This linearity is strongly affected by saturation of components in the system, the most obvious being the analog-to-digital converter. Given the high degree of uniformity among pixels, this linearity can easily be measured by illuminating the camera with a gradient of intensity. A plot of variance versus intensity should be linear. Such a plot is shown in Fig. 3 *A*. It is obvious from this figure that significant nonlinearities exist for the EMCCD camera. The deviation from linearity starts at <20,000 DL and is complex. If the highest amplifier gain is used, the read noise increases as well, but the only saturating component is the saturation of the analog-to-digital converter at 65,535 DL (Fig. 3 *B*). This allows for the use of the system up to ~40,000 DL.

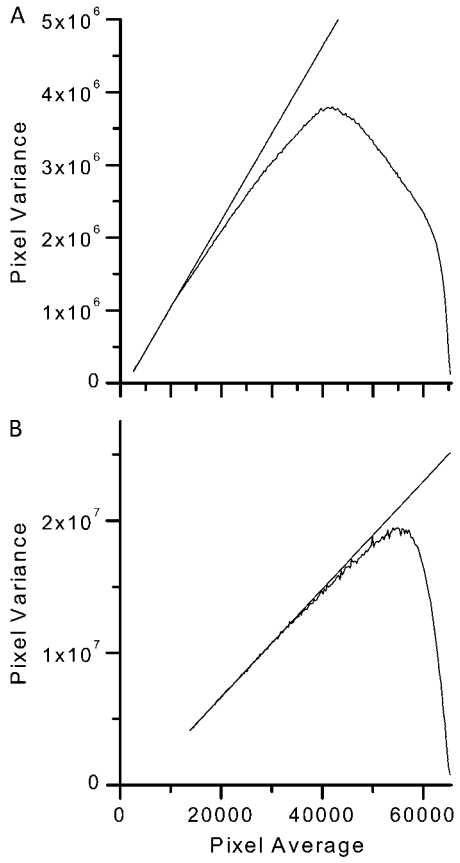

FIGURE 3 (*A*) Plot of variance versus intensity for a gradient of illumination on the Cascade camera with maximum electron multiplication and minimum analog-to-digital conversion gain. (*B*) Same plot as in *A*, but with maximum analog-to-digital conversion gain. Lines portray the slope of the initial part of the data.

Camera stability

Fig. 4 shows the value of the offset, *S* parameter, and readout noise variance as a function of time on the timescale of seconds and minutes. The data were collected starting when the camera had reached its equilibrium temperature as determined by the camera utility software. The *S* parameter quickly reaches an equilibrium value and remains relatively constant over 1 h. The read-noise variance shows a bit of a short-term trend, but this is at least two orders of magnitude smaller than the photon contributions to variance, and therefore does not contribute significantly. We have also observed that these parameters do not change significantly throughout the course of a day and are relatively constant from day to day (data not shown), though there is long-term drift associated with camera aging. Thus, these parameters can be calibrated at the beginning of a day and used throughout the day without change. Conversely, the offset parameter shows an exponential change at the beginning of each exposure sequence and must be corrected for in each measurement. This correction can be made using a region of the camera that is not illuminated during capture. In our situation, this is accomplished by blocking one of the dual-view channels. Alternatively, one can omit the data collected in the first 30 s of each exposure.

Dynamic range

To test the dynamic range of the camera system, we used 110-nm fluorescent beads diffusing freely in and out of a TIRF illumination field. Fig. 5 *A* shows the *B*/S versus $(\langle I\rangle - offset)/S$ plot for a 64 × 64-pixel region as a function of maximum average intensity. The image stacks were 1000 frames for this measurement. The plot is linear over *B*/*S* values from 1.08 to 9, corresponding to brightness values from 0.08 to 8, giving a dynamic range of 100 for the measurement. At high intensities, saturation becomes an issue and the plot deviates from linearity. Fig. 5 *B* shows the recovered n', which is also recovered accurately over the linear region of the system.

*G*1 analysis

As was mentioned in the Theory section, it is possible to avoid use of the *S* calibration factor if there is spatial or temporal redundancy in the acquisition. Fig. 6 *A* shows the temporal autocorrelation function for 110-nm beads diffusing into and out of a TIRF field. Fig. 6 *B* shows the spatial autocorrelation function in the *y* dimension for this same sample. The amplitude of the first point of the spatial autocorrelation is higher than the amplitude of the first point of the

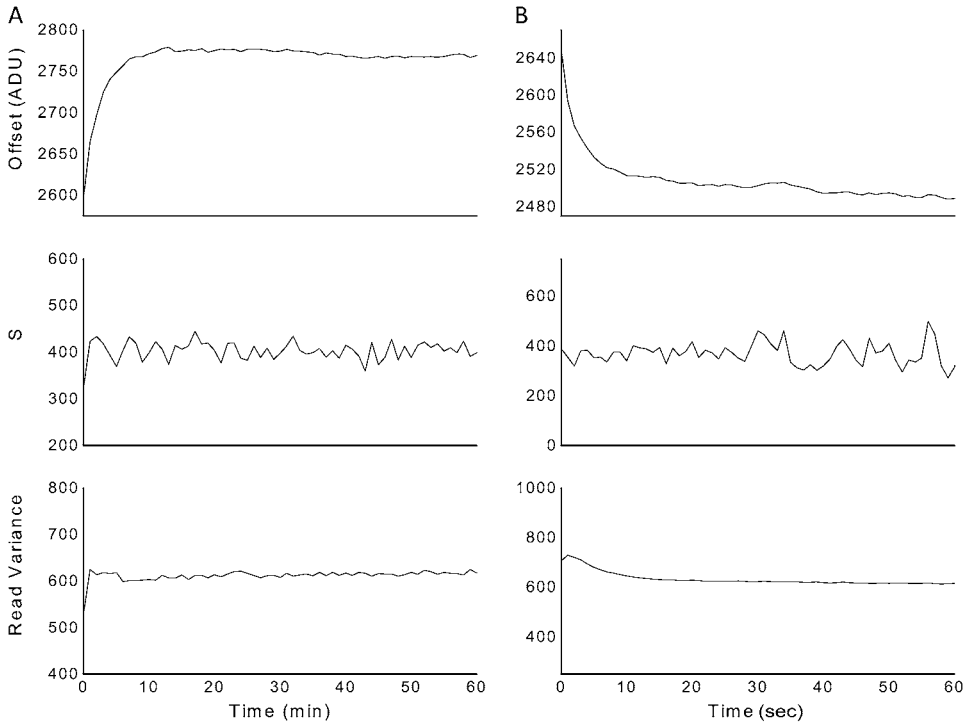

FIGURE 4 Plots of offset, read variance, and S parameter for the cascade camera as a function of time over (A) 60 s after 1 h warm-up time, and (B) 60 min starting at the end of camera cool-down.

temporal autocorrelation method, indicating that we are oversampling in space more than in time. Fig. 6 C shows a plot of B/S versus $(\langle I\rangle - offset)/S$ acquired using both the $G1$ and $G1y$ analysis methods. The brightness is higher for the spatial autocorrelation method, as suggested by the amplitudes of the spatial and temporal autocorrelation curves.

Camera exposure timing calibration

The Cascade 512B camera operates in two basic modes, overlap and nonoverlap. In the overlap mode, the camera is continuously exposed and the frame is transferred to the readout region of the camera each time a readout event is finished. In this way, the exposure time is defined by the readout time. In nonoverlap mode, the camera is cleared, exposed for the specified time, and finally transferred for reading. The only difference is the clearing step.

To elucidate more carefully the timing of the exposure sequence, we illuminated the camera with a diffraction-limited pulsed laser spot. The frequency of the laser was set slightly lower than the camera frame rate so that the laser pulse provides a reduced-frequency time-lapse series of the camera response. The laser pulse was a 100-μs square-wave and therefore will add a total of 100 μs to the observed camera exposure width. The exposure can be easily defined in terms of percentage of the camera period and then transformed into real time based on the known camera frame rate. Fig. 7 A shows a time series for a 375-μs exposure in nonoverlap mode. At time zero, the camera is cleared by shifting in new rows from the top of the camera, resulting in a smeared image on the upper half of the device. Throughout the exposure, the laser spot is seen in the center of the image. At the end of the exposure, the frame is transferred for readout, resulting in a smeared image on the lower half of the device. Fig. 7 B shows the measured exposure times, which agree very well with the exposure times set via software. A linear fit gives a slope of 0.99 with an intercept at 97 μs, as expected for this experiment. The exposure time for overlap mode is ~1 ms shorter than the total frame time, indicating that the shift process takes ~1 ms (data not shown). Photometrics lists the vertical shift rate for this camera at 2 μs/row, giving a total shift time of ~1 ms for the camera, in agreement with the observed behavior.

Given the high fidelity of the camera exposures, it should be possible to perform brightness analysis as a function of exposure time for confocal illumination of fast moving particles. Fig. 8 A shows brightness/exposure time as a function of exposure time for monomeric EGFP at 40 nM in buffer. The data fit well with Eq. 7 using the binning function in Eq. 10, giving a diffusion time of 120 $\pm$ 40 μs. The axial/radial ratio was fixed at 1:3, as expected for confocal detection (17). Given the diffusion coefficient of mEGFP (90 $\mu m^2/s$ (18)), this corresponds to a radial beam waist of 200 $\pm$ 40 nm, which is close to the expected diffraction-limited focal size for this microscope.

For acquisitions of areas larger than a few pixels, one expects the exposure time resolution to be a function of camera vertical shift rate. Fig. 8 B shows the brightness of 110-nm beads in a TIRF field as a function of exposure time using aperture illumination over ~64 pixels, as well as full-

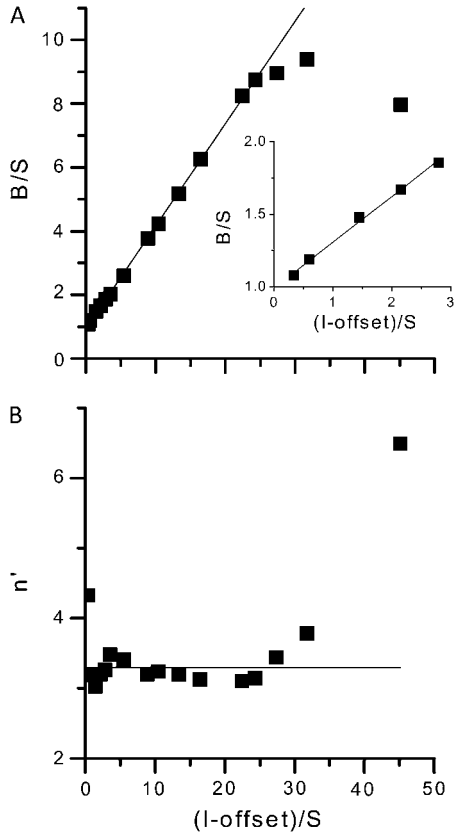

FIGURE 5 Plot of brightness (*A*) and particle number (*B*) as a function of intensity for 110-nm beads diffusing in a TIRF field. The brightness was changed by changing the laser power. For *A*, the lines are best fit to the linear region of the data. For *B*, the line represents the average over the linear region of the data.

frame illumination. The τ_z and r values were determined from the autocorrelation function using Eq. 11 (Fig. 8 *C*). The two plots are significantly different, indicating that illuminated area has a significant influence on exposure due to the shifting time of the camera. The lines show the expected brightnesses assuming that the brightness with 5300 μs exposure is unaffected by the vertical pixel shifts. The aperture illumination is much closer to the expected value than the full-field illumination, as expected due to the influence of the vertical shift rate.

Concentration independence of brightness measurement

Fig. 9 *A* shows a plot of recovered n' value for a serial dilution of EGFP in phosphate-buffered solution. The exposure time was set at 100 μs for this measurement. In addition, the laser was focused to a diffraction-limited spot within the sample. The plot is nicely linear, indicating that we are, in fact, recovering concentration independent of brightness. Fig. 9 *B* shows the recovered brightness, which is constant and independent of concentration.

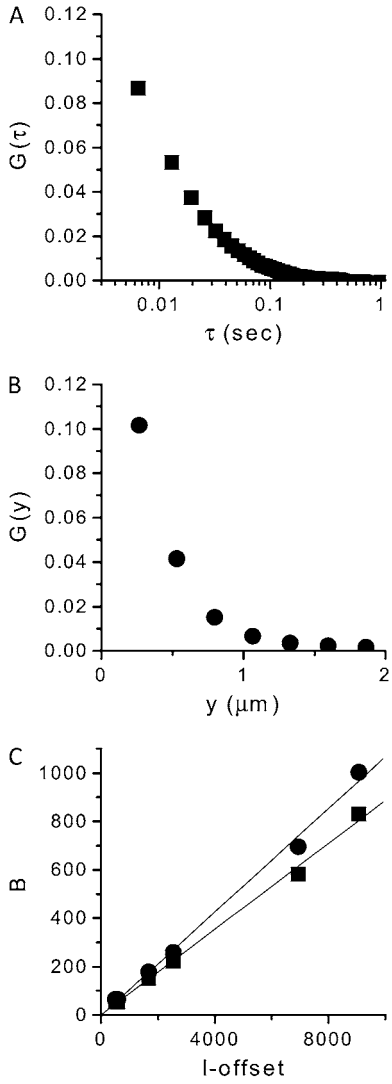

FIGURE 6 (*A* and *B*) Temporal autocorrelation function (*A*) and spatial autocorrelation in the *y* dimension (*B*) for 110-nm beads diffusing in a TIRF field. (*C*) Brightness as a function of intensity from the *G*1 (*circles*) and *G*1*y* (*squares*) analysis methods. Data were the same as in Fig. 5. For *C*, the lines are the best fit to the data.

Dynamic *N* and *B* measurements

Given the highly parallel nature of brightfield detection, it seems possible that *N* and *B* measurements could be analyzed as a function of time for a sample in which either brightness or concentration is changing. To demonstrate this, we measured DiOC16 in DOPC supported bilayers. DOPC forms a highly uniform bilayer with no liquid ordered domains at room temperature. Thus, it should provide a uniform brightness and concentration. In addition, at the intensities used in this study, the concentration of DiO bleaches out within 1 min. Therefore, if our technique works, we should see a decrease in concentration over time with no change in brightness.

Fig. 10 shows a time series of brightness versus intensity images for a hexagonally illuminated region of the bilayer. In

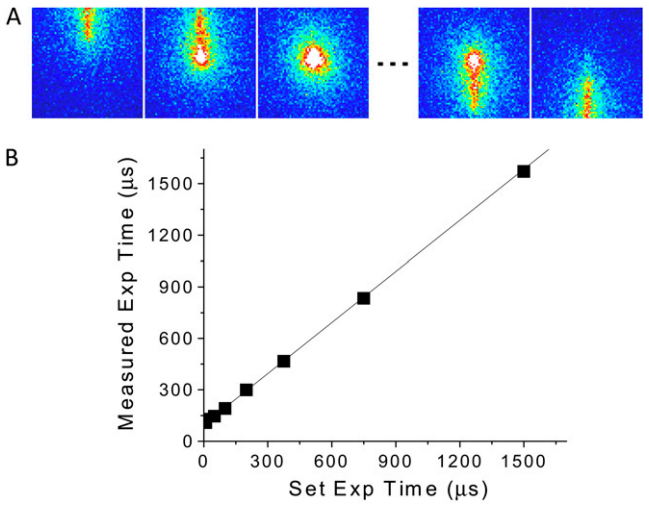

FIGURE 7 (*A*) Time-lapse images at the beginning, middle, and end of a 750-μs exposure as determined by pulsed laser illumination at a slightly lower frequency than the frame rate. (*B*) Plot of measured exposure time versus exposure time set via software. The line is the best fit to the data.

addition, a background component of 1500 DL per frame was subtracted as described in materials and methods. There appears to be an exponential decrease in overall intensity as a function of time for the system, whereas the brightness doesn't change significantly. Therefore, the intensity decreases are a result of concentration changes due to bleaching.

Due to the diffusion of the molecules, there should be a spatial concentration gradient with the fewest number of molecules in the center of the illuminated volume. Fig. 11 shows selected high- and low-intensity regions of the histogram and the corresponding regions of the image. High-intensity histogram points correspond to the outer region of the illuminated volume and low-intensity points correspond to the inner region, as predicted. In addition, a small ring at the edge of the illuminated volume is selected at low intensity. This is a result of the clipping of the point-spread function in this region, resulting in a reduced focal volume and thus a decrease in apparent particle number.

N and *B* analysis in living cells

Fig. 12 *B* shows the B/S versus $(\langle I\rangle - offset)/S$ histogram for two CHO K1 cells transfected with a GAP-EGFP construct. The histogram shows two distinct regions with equal brightness. Selection of the image pixels that correspond to these regions of the histogram shows that these spots correspond to two cells in the image with different transfection efficiencies of the GAP-EGFP. The average relative brightnesses of the high-intensity and low-intensity cell were 0.33 and 0.28 and the corresponding n' values were 150 and 39. If we assume a γ factor of 0.5, there are 74 particles/point-spread function in the bright cell and 20 particles/point-spread function in the dim cell. Fig. 12 *C* shows the 2D histogram for the cell after illumination for 50 s. The concentration has decreased significantly, especially for the brightest cell, but the brightness has not changed.

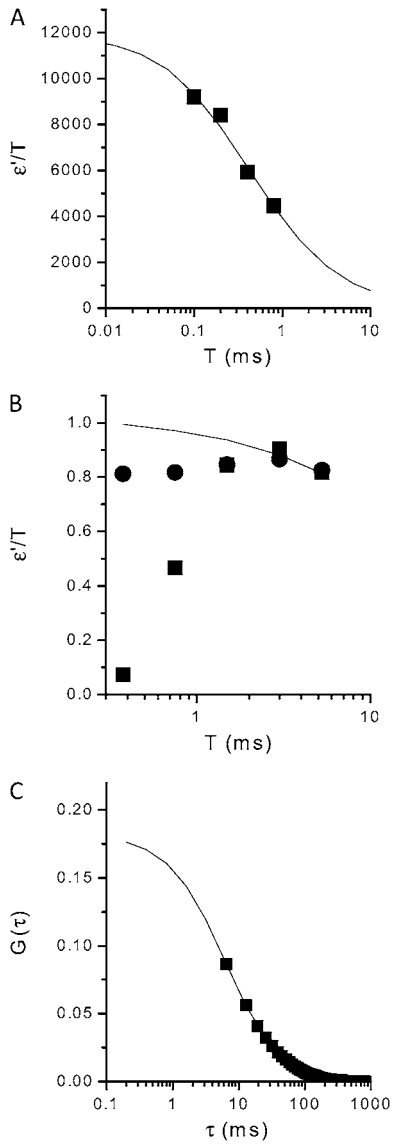

FIGURE 8 (*A* and *B*) Brightness divided by exposure time as a function of exposure time for (*A*) EGFP in solution with confocal excitation and (*B*) 110-nm beads in a TIRF field with full-field (*circles*) and apertured (*squares*) illumination. (*C*) Temporal autocorrelation function for the apertured data in *B*. For *A* and *C*, the solid line is the fit to the data to Eqs. 7 and 9. For *B*, the solid line is the expected brightness according to Eq. 7 extrapolated from the brightness at 5.3 ms exposure time, with the diffusion time determined from the autocorrelation function in *C*.

DISCUSSION

Camera characteristics

The *N* and *B* analysis method relies on the determination of variance and intensity from an image. It is important to scrupulously test the camera for stability and linearity. We have demonstrated that in terms of gain and readout noise, the

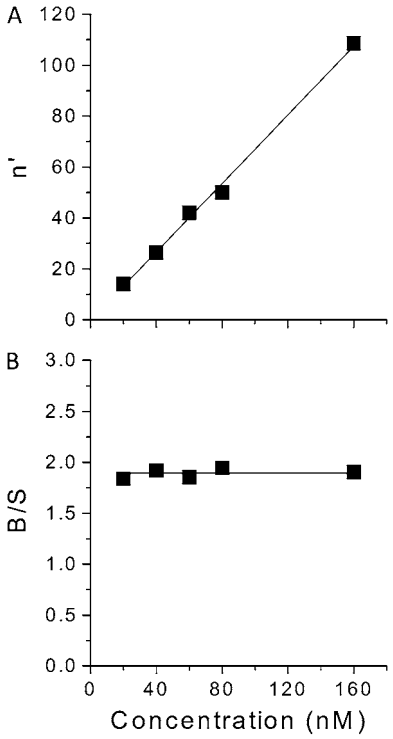

FIGURE 9 Number (*A*) and brightness (*B*) as a function of concentration for EGFP in solution with confocal excitation. For *A*, the line is the best fit to the data, and for *B*, the line represents the average of the data.

camera shows negligible drift over the timescale of a typical experiment (1 h). Also, we proved that there is a high degree of pixel uniformity. This uniformity is critical for producing accurate maps of particle number and brightness.

The offset of the camera shows drifts on timescales from seconds to minutes. In this study, we have corrected for this by using a nonilluminated region of the camera. Several camera manufacturers produce cameras with dynamic offset correction mechanisms. These cameras may provide a solution to this problem. A disappointing feature of the camera under study was the high degree of nonlinearity. A large portion of the camera's dynamic range is unusable because of this effect. Given these effects, it is crucial that any study using these methods test each camera for its stability and linearity.

To assess the relationship between the measurements made by the camera system and a photon-counting system with equivalent quantum efficiency, we performed simulations. The simulations demonstrate that the analog measurement of intensity and molecular brightness is reasonably equivalent to the photon-counting measurement in terms of signal/noise. The major differences in brightness error lie at low intensities. We have also shown that this is not a result of read-noise contribution, as simulations with no read noise do not have this problem (data not shown). We have also shown that for higher concentrations at the same brightness, the error becomes comparable to the photon-counting situation. Note that the high concentration data point has ~28 molecules in the focal volume. This is well within the range of physiological conditions as calculated from GAP-EGFP in the Results section.

Dynamic range

Previous studies have shown that an analog confocal system with a 12-bit analog-to-digital converter had a dynamic brightness range of ~20 (5). Here, we demonstrate that the camera-based system has a linear dynamic range of at least 100. The camera has a 16-bit analog-to-digital converter which accounts for the increase in dynamic range of almost an order of magnitude. The key limitation of the dynamic range for the system is the nonlinearity of the camera, which forced us to use the highest digital gain and therefore the lowest dynamic range. Nevertheless, simultaneously mea-

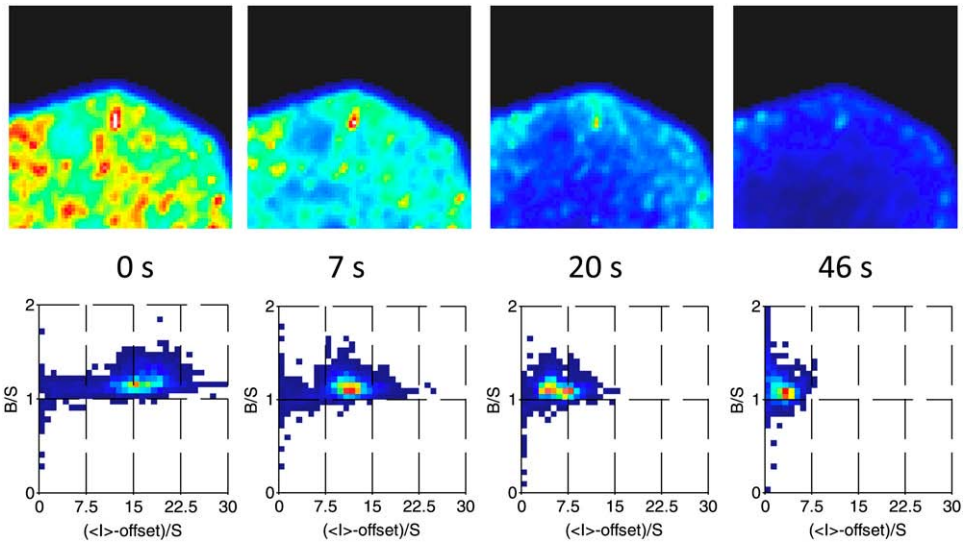

FIGURE 10 (*Upper*) Intensity images for DiOC16 in a DOPC planar supported bilayer at different time points after the start of illumination. The image size is 17 μm. (*Lower*) Brightness versus intensity histograms corresponding to the images in *A*.

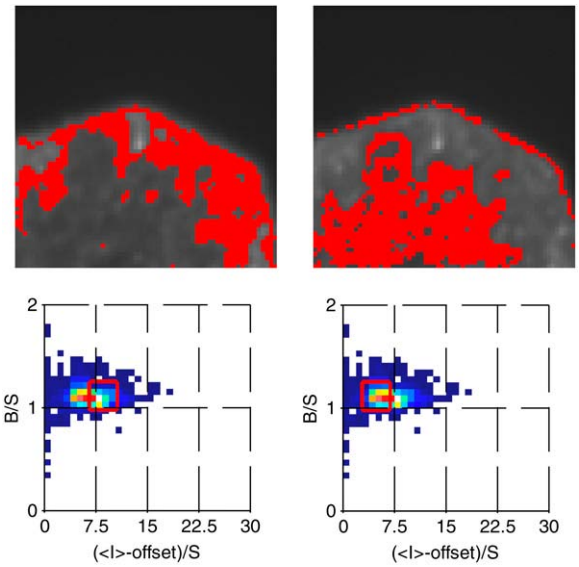

FIGURE 11 Images of the supported bilayer from Fig. 8 after 20 s of illumination. Red regions correspond to selected pixels from the B/S versus $(\langle I\rangle - offset)/S$ histogram.

suring particles with brightness ratios of >100 is unlikely. Therefore, this dynamic range is more than adequate for most biological aggregation measurements.

*G*1 analysis

Although accounting for the analog noise of the camera system is a straightforward process, it requires additional measurements and precautions that are not ideal for routine measurements. Shot noise has no time correlation and therefore could be removed by measuring the covariance of a pixel with itself at subsequent time points when the molecule has not moved significantly. This is equivalent to measuring the first point of the autocorrelation rather than the zeroth point, and therefore is referred to as $G1$ analysis. In the same way, one can use the spatial redundancy of oversampled acquisition and calculate the covariance of a pixel with neighboring pixels that show the same molecular information. This is equivalent to measuring the first point of the spatial autocorrelation function and is referred to as $G1y$ analysis. Both of these cases are shown in Fig. 6 for 110-nm beads diffusing in and out of a TIRF field. The spatial autocorrelation is oversampled to a greater extent than the temporal autocorrelation, and therefore, the $G1y$ analysis recovers a higher brightness than the $G1$ analysis. The relative accuracy of such methods will depend on the experimental setup, namely on resolution, magnification, and time resolution.

Camera timing

One distinct advantage of N and B analysis over traditional autocorrelation methods is the dependence on exposure time as opposed to overall acquisition rate. To accurately assess

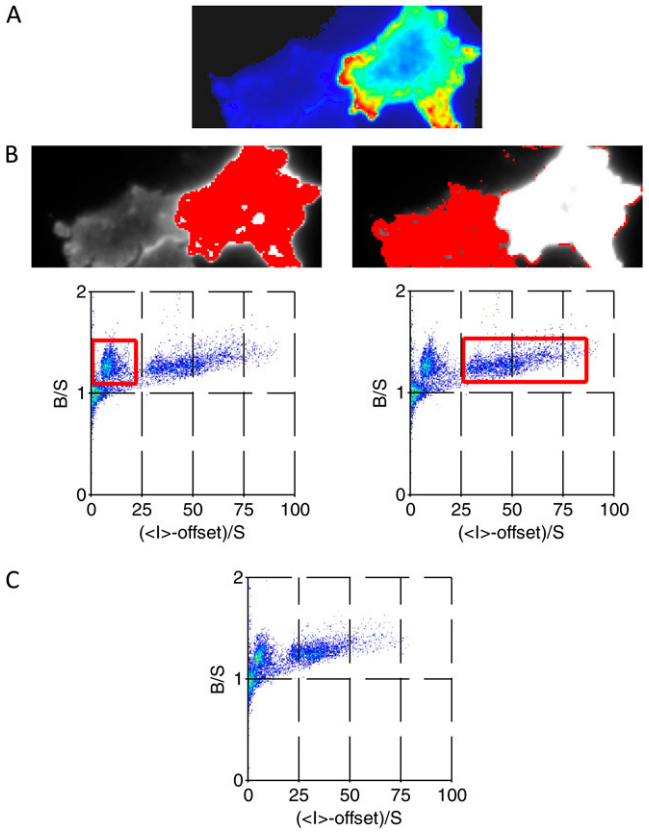

FIGURE 12 (A and B) Images of CHO K1 cells transfected with GAP-EGFP. (B) Red regions in A correspond to selected pixels from the B/S versus $(\langle I\rangle - offset)/S$ histograms. (C) B/S versus $(\langle I\rangle - offset)/S$ histograms after 50 s of illumination.

the number and brightness of a molecule that diffuses through the focal volume in 100 μs, one must have an exposure time on the order of 100 μs, but the acquisition rate could be much slower, perhaps 30 frames/s. This same concept applies to the $G1y$ analysis (but not the $G1$ analysis, as it relies on temporal redundancy). It is also important to note that the time between frames need not be conserved, as it is only the shape of the intensity that is important, not its time dependence. This should allow similar measurements to be done on spinning-disk confocal systems where the pixels are not sampled in a linear fashion.

To assess the exposure time of the EMCCD, we used a heterodyning approach with a pulsed diode laser. Although the exposure time is conserved quite accurately down to <100 μs, there is obvious vertical pixel shifting at the beginning and end of each exposure (Fig. 7). Therefore, it is possible to accurately measure the brightness of EGFP, which has a diffusion coefficient of 90 $\mu m^2/s$ (18) and a diffusion time through the focal volume of ~100 μs, but only with confocal excitation illuminating a few pixels of the camera (Fig. 8 A). Under these circumstances, the vertical shift has negligible effect on the exposure time, because the vast majority of the camera pixels experience no light

throughout the exposure. As the exposure time becomes significantly shorter than the diffusion time, one expects relatively little change in ε'/T. The solid line in Fig. 8 *B* shows how this behavior is borne out in the theory of the dependence of brightness on exposure time (Eq. 7). From the black squares in Fig. 8 *B*, we can see that illumination of the entire camera for TIRF excitation of fluorescent beads leads to a significant underestimation of the brightness below a few milliseconds. This is likely due to spatial shifting of the camera. The overall shift time of the camera is 1 ms, which is consistent with our observations. Fortunately, one can illuminate a somewhat smaller (64-pixel) vertical portion of the camera and resolve the brightness much more accurately down to fractions of a millisecond, as observed for apertured illumination (Fig. 8 *B*, *circles*). With our microscope setup, this apertured region is $\sim$17 μm in size. A typical cell is $\sim$10 μm in diameter and should be amenable to such analyses.

Concentration independence of brightness

In Fig. 9, we performed a serial dilution of EGFP in buffer. The number of particles tracks linearly with the known concentration while the brightness remains constant, confirming the efficacy of our technique for such measurements. The resolved concentrations are on the order of 100 nM. This is similar to native expression levels for many cellular proteins. Therefore this technique should be well suited to such measurements.

Supported bilayer experiments

As a model system for membrane diffusion, we chose a DOPC supported planar bilayer doped with DiOC16. The DiOC16 molecular brightness is easily resolved above background ($B/S = 1$) in only 3.25 s of acquisition (500 frames) on a 64 $\times$ 64 pixel region. The supported bilayer provides another opportunity to verify the concentration independence of the brightness measurement. Due to the slow diffusion of the membrane-confined molecules, photobleaching occurs rapidly, so that after 1 min of acquisition, the fluorophore is completely depleted from the center of the illuminated volume. The ability to resolve the brightness within a few seconds allows for tracking of this process. The intensity decreases exponentially with the decrease in number of particles, whereas the brightness remains constant throughout the process. It is important to note that a nonbleached background will become predominant as bleaching occurs and therefore must be subtracted from the average and variance before calculating the brightness. In our case, the background corresponds to 1500 DL, $>$10% of the overall intensity at time zero. Nevertheless, simple subtraction removes this background contribution from the measurement.

Although the average number of molecules/diffraction-limited volume is 14 at the 20-s time point, it is straightforward to see from the average image that the intensity is not uniform over the field of view. Therefore, we should be able to resolve spatial differences in particle number. A look at the brightness versus intensity histogram for this time point shows that the distribution is broader over the intensity axis than the brightness axis. The pixels that correspond to high intensity in the histogram also correspond to the edges of the illuminated area, which are expected to have higher concentration.

Live-cell experiments

Although supported membranes are excellent model systems for the study of single-molecule diffusion, they bear a limited resemblance to live cells, where diffusion is quite likely anomalous and concentrations are heterogeneous. Therefore, we undertook measurements on live CHO K1 cells expressing GAP-EGFP. This protein is monomeric in the basal membrane (15). Fig. 12 *A* shows two cells expressing vastly different amounts of the construct. Nevertheless, their brightnesses are identical and easily resolved from the background, demonstrating the appropriateness of this technique for measuring single-molecule brightnesses independent of concentration for living cells. The observed concentrations are within the range shown to demonstrate the best signal/noise according to our simulations. The standard deviation in the brightness distribution for both cells was 0.09. Given an average brightness of 0.3 for both cells, this is well within the necessary range for observation of oligomerization. Given the strong dependence of the TIRF illumination on distance from the surface, one might expect spatial deviations in brightness due to membrane undulations. This is not observed, suggesting that either these undulations are uniform and below the resolution of the measurement or the undulations are of insignificant amplitude to influence the measurement. In either case, they cause a small enough perturbation that measurements of oligomerization would not be affected. In addition, extended bleaching of the cells shows significant changes in intensity but not in brightness (Fig. 12 *C*). If the GAP-EGFP were multimeric in the cell membrane, one would expect to see the brightness change with photobleaching as EGFP tags on the multimeric species are bleached one by one until the multimer appears monomeric, containing only one fluorescent EGFP.

CONCLUSION

Given the highly parallel nature of camera data acquisition and the single-molecule sensitivity of EMCCD cameras, it is desirable to characterize them for molecular brightness measurement. We have shown that these devices present significant challenges in terms of drift and nonlinearity. The drift issue can be easily overcome through real-time subtraction methods. The nonlinearity issue persists, and it severely limits the dynamic range of acquisition. Nevertheless, we show that even with this limitation, the dynamic range is almost an order

of magnitude greater than that seen previously for analog detectors used in confocal microscopy. The timing of the camera exposures has also proven to be complex, with a significant spatial dependence. Nevertheless, with an illumination aperture larger than that of a typical living cell, the timing is maintained to submillisecond exposures, which is fast enough for observation of most cellular processes. The parallel acquisition of the EMCCD compared with confocal measurements has proven to be quite fruitful, allowing for accurate determination of brightness as a function of time and space in the presence of significant concentration heterogeneity. This allows for real-time monitoring of particle number and brightness in living cells. This technique holds great promise for elucidating dynamic and complex protein-protein interactions that form the basis for important cellular processes.

APPENDIX

In an analog detection system, it is not photon counts that are detected, but rather pulses of photocurrent. For most analog detectors, the photon pulse height distribution is quasiexponential. This is a result of the probabilistic nature of photon multiplication, where several electron impact events have a similar probability of generating secondary electrons. In addition, the amplifier and analog-to-digital converter in the system contribute a readout noise that is Gaussian. Fig. 13 shows the pulse height distribution for the 512B camera in the dark at full gain. A fit of the distribution to a Gaussian plus that Gaussian convoluted with a multiexponential function is shown in red. The read noise standard deviation is 26 DL with an average single-photon intensity (gain) of 130 DL.

The addition of independent random variables (convolution) results in an average and variance that are the sums of the average and variance of such variables. As a result, the offset and read noise variance can simply be subtracted from the average and variance, leaving only the gain-dependent single-photon pulse height distribution. This distribution is the photon probability-weighted sum of the k photon probability distributions as follows:

$$P(I) = \sum_{k=0}^{\infty} PCH(k)P^{k}(I). \tag{12}$$

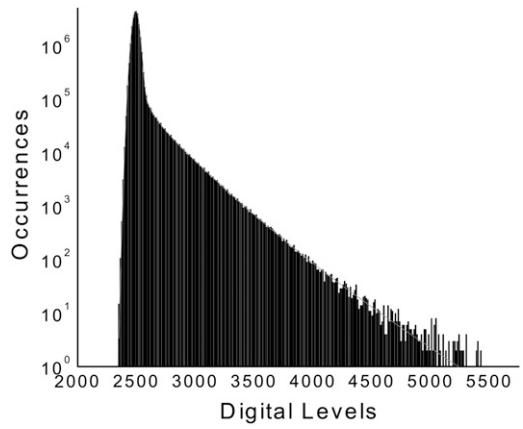

FIGURE 13 Histogram of dark intensities for Cascade 512B camera with a maximum electron multiplication gain and maximum analog-to-digital gain, along with a fit (*red line*) to the model described in the Appendix.

Here $PCH(k)$ is the photon-counting histogram as described previously (2). Its specific form is not important for this derivation. In turn, the individual k photon probability distributions are generated from the single-photon analog probability distribution through multiple convolutions:

$$P^{k}(I) = P^{1}(I) \otimes P^{k-1}(I). \tag{13}$$

As mentioned previously, the variance of convoluted functions is the sum of the individual variances. As a result, the k photon variance is simply $k \times V_a$ where V_a is the analog single-photon variance.

When distributions are added (as in Eq. 12), the variance is only additive when the distribution averages are equal. This is not the case with the k photon analog distributions. As a result, Eq. 12 must be solved in terms of the average intensity squared (raw moment as opposed to central moment), which is additive for shifted distributions. One can easily show that this value is given as

$$\langle I^2 \rangle = V_a \langle I \rangle + G^2 \langle I^2 \rangle, \tag{14}$$

where G is the analog gain, which is given by the average intensity of the single-photon pulse-height distribution ($\langle I \rangle = \langle k \rangle G$). Using the standard definition of variance, we obtain the final equation for the analog variance in terms of the average photon counts and PCH variance:

$$\sigma^2 = V_a \langle k \rangle + G^2 Var(PCH). \tag{15}$$

For a single species, the average photon counts are given by the brightness times the occupation number (εn) and the variance is given by $Var(PCH) = \gamma \varepsilon^2 n + \varepsilon n$, where γ is a point-spread function shape factor given by the normalized integral over the point-spread function squared (3). The analog variance can then be written in terms of number and brightness as

$$\sigma^2 = (V_a + G^2)\varepsilon n + G^2 \gamma \varepsilon^2 n. \tag{16}$$

It is not trivial to measure the single-photon variance; therefore, we define a parameter S that is given by the slope of an intensity versus variance plot for a light source with constant intensity (no temporal fluctuations). Such a light source would give a Poisson photon counting signal and it is easy to derive the value of S from Eq. 4:

$$S = \frac{V_a}{G} + G. \tag{17}$$

Incorporating the read variance and offset, the analog variance and intensity are then given by

$$\sigma^2 - \sigma_0^2 = SG\varepsilon n + G^2 \gamma \varepsilon^2 n \tag{18}$$

and

$$\langle I \rangle = G\varepsilon n. \tag{19}$$

We thank Michelle Digman for providing the soluble EGFP and Alan Horwitz for providing the GAP-EGFP plasmid.

We also acknowledge National Institutes of Health grants P41 RR03155 and RO1 DK066029, which provided funding for this work.

REFERENCES

1. Quian, H., and E. L. Elson. 1990. Distribution of molecular aggregation by analysis of fluctuation moments. *Proc. Natl. Acad. Sci. USA*. 87:5479–5483.
2. Chen, Y., J. D. Müller, P. T. C. So, and E. Gratton. 1999. The photon counting histogram in fluorescence fluctuation spectroscopy. *Biophys. J.* 77:553–567.
3. Müller, J. D. 2004. Cumulant analysis in fluorescence fluctuation spectroscopy. *Biophys. J.* 86:3981–3992.

4. Digman, M. A., R. Dalal, A. F. Horwitz, and E. Gratton. 2008. Mapping the number of molecules and brightness in the laser scanning microscope. *Biophys. J.* 94:2320–2332.

5. Dalal, R., M. A. Digman, A. F. Horwitz, V. Vetri, and E. Gratton. 2007. Determination of particle number and brightness using a laser scanning confocal microscope operating in the analog mode. *Microsc. Res. Tech.* 71:69–81.

6. Kolin, D. L., D. Ronis, and P. W. Wiseman. 2006. k-Space image correlation spectroscopy: a method for accurate transport measurements independent of fluorophore photophysics. *Biophys. J.* 91:3061–3075.

7. Burkhardt, M., and P. Schwille. 2006. Electron multiplying CCD based detection for spatially resolved fluorescence correlation spectroscopy. *Opt. Express.* 14:5013–5020.

8. Kannan, B., L. Guo, T. Sudhaharan, S. Ahmed, I. Maruyama, and T. Wohland. 2007. Spatially resolved total internal reflection fluorescence correlation microscopy using an electron multiplying charge-coupled device camera. *Anal. Chem.* 79:4463–4470.

9. Kannan, B., J. Y. Har, P. Liu, I. Maruyama, J. L. Ding, and T. Wohland. 2006. Electron multiplying charge-coupled device camera based fluorescence correlation spectroscopy. *Anal. Chem.* 78:3444–3451.

10. Sisan, D. R., R. Arevalo, C. Graves, R. McAllister, and J. S. Urbach. 2006. Spatially resolved fluorescence correlation spectroscopy using a spinning disk confocal microscope. *Biophys. J.* 91:4241–4252.

11. Petersen, N. O., P. L. Höddelius, P. W. Wiseman, O. Seger, and K. E. Magnusson. 1993. Quantitation of membrane receptor distributions by image correlation spectroscopy: concept and application. *Biophys. J.* 65:1135–1146.

12. Wu, B., and J. D. Müller. 2005. Time-integrated fluorescence cumulant analysis in fluorescence fluctuation spectroscopy. *Biophys. J.* 89:2721–2735.

13. Hassler, K., M. Leutenegger, P. Rigler, R. Rao, R. Rigler, M. L. Gösch, and T. Lasser. 2005. Total internal reflection fluorescence correlation spectroscopy (TIR-FCS) with low background and high count-rate per molecule. *Opt. Express.* 13:7415–7423.

14. Zacharias, D. A., J. D. Violin, A. C. Newton, and R. Y. Tsien. 2002. Partitioning of lipid-modified monomeric GFPs into membrane microdomains of live cells. *Science.* 296:913–916.

15. Wiseman, P. W., C. M. Brown, D. J. Webb, B. Hebert, N. L. Johnson, J. A. Squier, M. H. Ellisman, and A. F. Horwitz. 2004. Spatial mapping of integrin interactions and dynamics during cell migration by image correlation microscopy. *J. Cell Sci.* 117:5512–5534.

16. Burns, A. R., D. J. Frankel, and T. Buranda. 2005. Local mobility in lipid domains of supported bilayers characterized by atomic force microscopy and fluorescence correlation spectroscopy. *Biophys. J.* 89:1081–1093.

17. Hess, S. T., and W. W. Webb. 2002. Focal volume optics and experimental artifacts in confocal fluorescence correlation spectroscopy. *Biophys. J.* 83:2300–2317.

18. Terry, B. R., E. K. Matthews, and J. Haseloff. 1995. Molecular characterisation of recombinant green fluorescent protein by fluorescence correlation microscopy. *Biochem. Biophys. Res. Commun.* 217:21–27.